

# SOURCE DETECTION IN SIMULATED XMM-NEWTON OBSERVATIONS

J. Rasmussen<sup>1</sup>, K. Pedersen<sup>1</sup>, and M. Götz<sup>2</sup>

<sup>1</sup>Astronomical Observatory, University of Copenhagen, Juliane Maries Vej 30, DK-2100 Copenhagen Ø, Denmark

<sup>2</sup>Theoretical Astrophysics Center, Juliane Maries Vej 30, DK-2100 Copenhagen Ø, Denmark

## ABSTRACT

We present preliminary results from our on-going study: Comparing and optimizing source detection procedures for XMM images. By constructing realistic spatial and spectral source distributions and “observing” these through the XMM Science Simulator we study how source characteristics and instrumental effects influence detection. We are currently undertaking a statistical analysis on the outcome of running source detection algorithms on the simulated EPIC pn and MOS images in various energy bands. Particular emphasis is on the efficiency and reliability for detecting the faint, extended emission from distant clusters of galaxies. Here we present simulated EPIC images applicable to the XMM Large-scale Structure Survey (10 ksec pointings of “blank fields”). However, we emphasize that our procedure is flexible, including as many realistic source characteristics and instrumental effects as possible, and yet modest in computational demand. As such it can be used for simulating XMM data obtained from virtually any X-ray source.

All simulation products are made available at our website (<http://www.astro.ku.dk/xcosmos/>).

Key words: Missions: XMM-Newton – methods: data analysis – X-rays: galaxies: clusters – X-rays: general

## 1. INTRODUCTION

One of the main goals of the XMM Large-Scale Structure Survey (XMM LSS) (Pierre et al. 2001) is to map the large-scale distribution of X-ray selected galaxy clusters out to a redshift of  $\sim 1$  and to detect the richest clusters out to a redshift of  $\sim 2$ . Since the detection of faint, extended sources from X-ray data is a crucial part of the XMM LSS project, an efficient and reliable source detection method must be implemented for the survey.

Previous investigations (Valtchanov et al. 2001; Regier et al. 2001) have invoked simplified source field setups and left out some instrumental effects, when studying the efficiency of various detection algorithms on simulated XMM images and estimating, e.g., completeness and confusion limits. By using schematic as well as more realistic source fields and by a more complete treatment of instrumental effects through the XMM Science Simulator soft-

ware SCISIM (which mimics the performance of XMM by ray-tracing incoming photons through the mirror and detector systems), we extend this earlier work and address additional questions, like

- What is the optimum energy band for distant cluster detection in XMM LSS data?
- How does cluster X-ray morphology and off-axis distance influence detection and photometric reconstruction of source properties?
- How does one deal effectively with, e.g., blending of extended and pointlike sources and removal of bright point sources?

Here we present a few simulated 10 ksec XMM EPIC images being used for comparing and developing source detection procedures for the XMM Large Scale Structure Survey.

## 2. THE SIMULATION SETUP

### 2.1. SOURCE FLUXES

Three types of objects are considered, AGN type 1 and 2 and groups/clusters. Point source (i.e. AGN) fluxes and object types are based on the X-ray Background (XRB) synthesis model of Gilli et al. (2001), down to a limiting flux of  $1.3 \times 10^{-15}$  erg cm<sup>-2</sup> s<sup>-1</sup> (0.5–2 keV). This XRB model is consistent with the projected cumulative number density  $N$  of sources as a function of X-ray flux  $S$  (the logN-logS relation) as derived from deep XMM (Hasinger et al. 2001) and Chandra (Tozzi et al. 2002) observations. For clusters and groups, fluxes are provided by the assumed mass-temperature ( $M - T$ ; see below) and luminosity-temperature ( $L_X - T$ ) relations down to  $5 \times 10^{-15}$  erg cm<sup>-2</sup> s<sup>-1</sup> (0.5–2 keV).

We have produced two sets of simulations, distinguished only by the assumed cluster properties. In the first set, clusters are drawn from standard Press-Schechter (P-S) realizations of halos in a flat  $\Lambda$ CDM cosmology with  $\Omega_m = 0.3$ ,  $\sigma_8 = 0.94$  and  $H_0 = 65$  km s<sup>-1</sup> Mpc<sup>-1</sup>. They are extracted from 100 Monte Carlo realizations of the redshift interval  $z = 0 - 2$  down to a mass floor of  $10^{13} M_\odot h_{100}^{-1}$ , assuming the  $M - T$  relation of Eke et al. (1996) and a non-evolving (local) cluster  $L_X - T$  relation of  $L_X \propto T^3$  (Borgani et al. 1999) with no intrinsic dispersion. To incorporate the observed  $L_X - T$  dispersion as well as the steepening of the  $L_X - T$  relation at low  $T$  ( $\leq 1$  keV),

cluster fluxes are “corrected” for these effects by assuming  $L_X \propto T^{\alpha \pm \sigma}$ , where  $\sigma$  is the standard deviation of a Gaussian distribution centered at  $\alpha$ . For  $T > 1$  keV,  $\alpha = 3$  and  $\sigma = 0.15$  is assumed (consistent with results from ROSAT cluster surveys, cf. Borgani et al. 1999), while  $\alpha = 5$  and  $\sigma = 1.0$  is taken for  $T < 1$  keV, based on galaxy group observations (Helsdon & Ponman 2000; Xue & Wu 2000). The cluster flux limit of  $5 \times 10^{-15}$  erg cm $^{-2}$  s $^{-1}$  is imposed hereafter.

The second set of simulations is based on a cosmological N-body simulation, from which five fields covering  $2.9 \times 2.9$  deg $^2$  and the redshift interval  $z \leq 1.4$  were extracted. Except for  $\sigma_8 = 1.0$ , other parameters are as above. Clusters are identified among the  $\sim 1.3 \times 10^6$  dark matter particles in each field via a friends-of-friends algorithm (where gravitationally unbound particles are removed) and drawn from a random  $30' \times 30'$  sight line through one of the fields. The  $L_X - T$  relation, including scatter as above, is here assumed to evolve such as to mimic no evolution in an ( $\Omega_m = 1, \Omega_\Lambda = 0$ ) universe, i.e.  $L_X \propto T^3 (d_L/d_L^*)^2$ , where  $d_L$  is the luminosity distance in an ( $\Omega_m = 0.3, \Omega_\Lambda = 0.7$ ) universe and  $d_L^*$  is the corresponding value in an ( $\Omega_m = 1, \Omega_\Lambda = 0.0$ ) cosmology.

A low-redshift cut at  $z = 0.1$  is imposed for computational reasons, excluding  $\sim 2\%$  and  $< 1\%$  of the input clusters from the P-S and N-body calculations, respectively (i.e. in most LSS fields, such nearby groups/clusters will not appear).

## 2.2. SPATIAL FLUX DISTRIBUTIONS

AGN are assumed to be pointlike, whereas cluster surface brightness distributions follow a 2-D  $\beta$ -profile of core radius  $r_c$ . Since there is to some extent a ‘degeneracy’ in the observational determination of  $\beta$  and  $r_c$ , we choose to fix  $r_c$  and let only  $\beta$  vary. For each cluster, values of  $\beta$  and the ratio  $\eta$  between minor and major isophote axis are drawn from observed distributions (Mohr et al. 1995), assuming these to be Gaussians of mean 0.65 and  $\sigma = 0.16$  ( $\beta$ ), and mean 0.80,  $\sigma = 0.12$  ( $\eta$ ).  $r_c$  is fixed at  $1/4$  of the cluster radius, which is determined through the angular diameter distance relation assuming X-ray emission out to  $r_{500}$ . The latter is directly provided by the simulations in the N-body case, while it is calculated for the P-S clusters in the point mass approximation.

Groups and clusters are each represented by an ensemble of point sources spaced  $2''$  apart, i.e. well below the on-axis PSF of FWHM  $\simeq 6''$  (the in-flight measured mean value for the three X-ray telescopes at  $E = 1.5$  keV; Jansen et al. 2001).

## 2.3. SOURCE AND BACKGROUND SPECTRA

All sources are assigned a spectrum, with normalizations provided by the XRB model for point sources and by the P-S/N-body simulations for clusters. The latter are

assigned an XSPEC-based *mekal* spectrum of metallicity  $Z = 0.25Z_\odot$ , with temperature and redshift provided by the cosmological simulations. For the AGN, a power law spectrum is assumed, i.e.  $I(E) \propto E^{-\Gamma}$ . In consistency with observations (e.g., Page 1998), we choose  $\Gamma = 1.7$  for AGN1, while AGN2 are assigned a value  $\Gamma = 1.8$  and an intrinsic H I column density of  $10^{22}$  cm $^{-2}$ . Given the spectral normalization in one band of the XRB model (e.g. 0.5-2 keV) this choice of spectra approximately reproduces the point source density predicted in the other model bands (2-10 and 5-10 keV).

A uniform diffuse X-ray background is added, modeled as a sum of two power laws. From fits to XRB observations we choose  $\Gamma = 1.4$  and a normalization  $A$  at  $E = 1$  keV of  $9.0$  keV cm $^{-2}$  s $^{-1}$  sr $^{-1}$  keV $^{-1}$  for the power law dominating the XRB spectrum above  $E \sim 1$  keV. This effectively acts in the simulations as the integrated contribution of sources fainter than our adopted flux limit. A second power law of  $\Gamma = 3.0$  and  $A = 1.0$  is also included, to account for the observed excess of emission at low energies (e.g., Miyaji et al. 1998; Parmar et al. 1999) compared to that expected from the  $\Gamma = 1.4$  power law. Adding this component also ensures an overall 1 keV normalization of  $10.0$  keV cm $^{-2}$  s $^{-1}$  sr $^{-1}$  keV $^{-1}$ , consistent with most XRB measurements (e.g., Chen et al. 1997).

Both individual sources and the X-ray background are subjected to a uniform absorbing column density of  $3 \times 10^{20}$  cm $^{-2}$ , which is the mean value expected for the XMM LSS 10 ksec pointings. On top of this the in-orbit measured particle and internal background is added, using normalizations as given in the XMM-Newton Users’ Handbook<sup>1</sup> and spectra roughly modeled as power laws including Gaussian representations of the four and two most prominent lines for the pn and MOS cameras, respectively (see also Katayama et al. 2002; a more detailed background model is soon to be implemented). This background component is not subject to mirror vignetting and hence not included in the input to SCISIM.

## 3. DATA “REDUCTION”

Simulated data are created for the EPIC MOS and pn CCD’s (with thin filters) using an exposure time of 10 ks, with all CCD’s in full frame mode. Spacecraft effects such as drift and jitter are neglected. The output of SCISIM is, in accordance with real XMM data, in the form of Observation Data Files (ODF’s) which include photon event files for each detector and CCD chip. Images and exposure maps are created from the event files using the XMM Science Analysis System (XMMAS).

For illustration purposes a source field image is produced for each simulation. These are convolved with a  $6''$  Gaussian and have image borders conforming to the field of view covered by the EPIC pn CCD’s.

<sup>1</sup> [http://xmm.vilspa.esa.es/user/AO2/uhb/xmm\\_uhb.html](http://xmm.vilspa.esa.es/user/AO2/uhb/xmm_uhb.html)

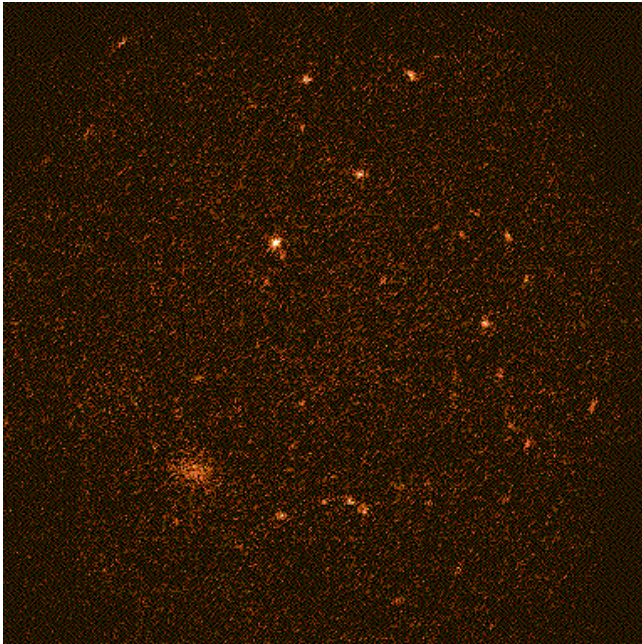


Figure 1. Simulated 0.5–2 keV image (photon counts for *pn+ 2MOS*; logarithmic intensity scale). Spatial scale is  $28' \times 28'$ .

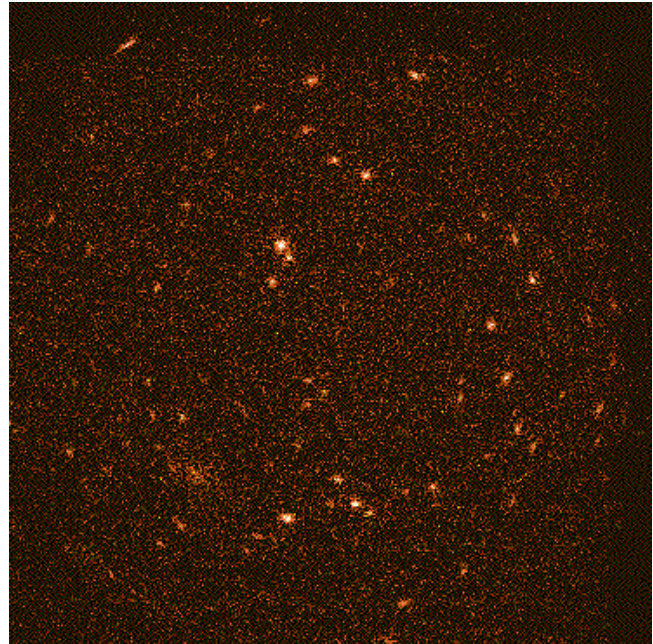


Figure 2. As Fig. 1, but for the 2–10 keV band.

#### 4. SIMULATION RESULTS AND SOURCE DETECTION

In Figures 1 and 2 we present examples of simulated EPIC images. These are “raw” 10 ksec photon count images, produced using the latest version (v3.0.0) of SCISIM with the XMM Current Calibration Files as of Dec 11, 2001, and with the P-S prescription for extended sources (§2.1). For comparison, the corresponding input source field is shown in Figure 3. In this particular representation, most clusters are “group-like”, with only two of the 12 input clusters having temperatures  $T > 3$  keV. The brightest one, a  $T = 3.3$  keV cluster at  $z = 0.35$  with a 0.5–2 keV flux of  $8 \times 10^{-14}$  ergs  $\text{cm}^{-2}$   $\text{s}^{-1}$ , stands out in the lower left corner.

Based on the simulated images, we have done preliminary tests of the performance of the wavelet-based XMM-SAS source detection task *ewavelet*, using wavelet scales of 2, 4, 8, 16, and 32 pixels, and a detection significance threshold of  $6\sigma$ . This method was chosen as a starting point because it was demonstrated to work reasonably well for the simulated XMM images of Valtchanov et al. (2001), and in this case, loosely judged, achieved optimum performance with the above parameters. A result of running this specific setup of *ewavelet* on the 0.5–2 keV image of Fig. 1 is illustrated in Figure 4, showing the wavelet-reconstructed image. Inspection of this image readily shows that four extended sources have been “detected”. Comparing the result with the input source field in Fig. 3 reveals that one of these extended sources (the most central one) is actually two point sources blended

together, whereas another results from the blending of two *extended* sources (this is not surprising, as one of these blended clusters is quite faint, being just above the adopted input flux limit of  $5 \times 10^{-15}$  ergs  $\text{cm}^{-2}$   $\text{s}^{-1}$ ). However, the brightest cluster mentioned above is safely detected, and a relatively faint ( $7 \times 10^{-15}$  ergs  $\text{cm}^{-2}$   $\text{s}^{-1}$ ),  $T = 3$  keV cluster at  $z = 1.01$  is also found. The remaining extended sources are apparently either too faint, too far off-axis (clearly the case for at least five of them), or suffer too much blending with bright point sources to be detected in this case. We further note in passing that the number of point sources detected roughly corresponds to half the input number — and this will certainly improve when including the results based on the 2–10 keV image.

#### 5. OUTLOOK

The simulated 10 ksec EPIC images, examples of which have been shown in this paper, will provide a baseline for testing and optimizing cluster detection procedures for the XMM Large Scale Structure Survey. This will, among other things, allow us to firmly address the questions posed in the introduction.

The detection of the  $z \simeq 1.0$  cluster described above seems particularly promising with respect to achieving our goal of finding high-redshift galaxy clusters, as it suggests that at least certain, reasonably massive but distant ( $z > 1$ ) clusters could be well within the reach of detection in the XMM LSS Survey (and other blank field XMM exposures of similar depth). It should also be emphasized in this context that work still remains in order to opti-

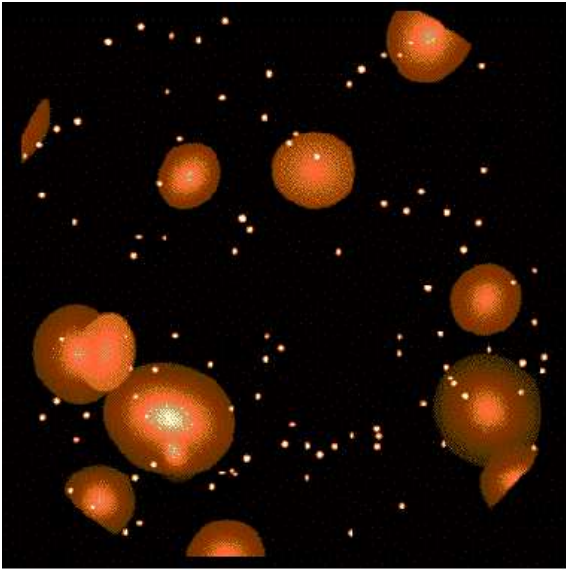


Figure 3. Input source field, corresponding to the simulated images shown in Figures 1 and 2.

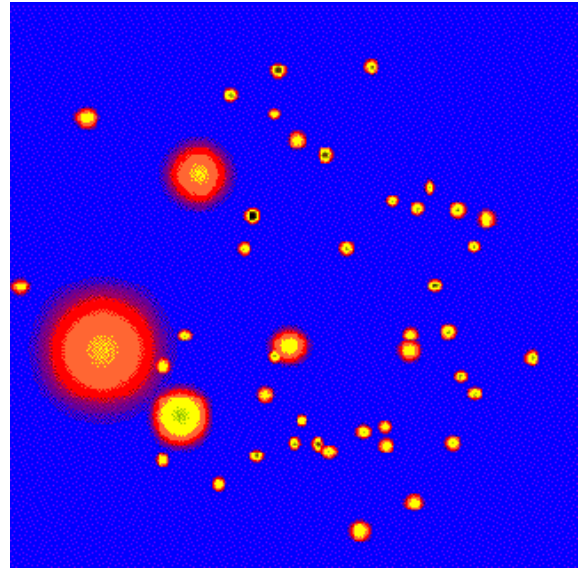


Figure 4. Wavelet reconstruction of the image shown in Fig. 1, illustrating the sources detected above a  $6\sigma$ -significance.

mize the method described here for the specific case of our simulated images.

A comprehensive analysis is currently being carried out involving additional detection algorithms, and we are also testing how selected methods for image restoration (including the publicly available version of the PIXON code; <http://www.pixon.com>) prior to source detection may improve detection performance. Further plans for the near future include testing source detection on deeper simulated exposures and to study how combining partially overlapping exposures will enhance detection. Results of this work will be presented in a forthcoming paper.

#### ACKNOWLEDGEMENTS

We thank R. Gilli for providing a numerical table of the XRB synthesis model published in Gilli et al. (2001).

#### REFERENCES

- Borgani S., Rosati P., Tozzi P., Norman C., 1999, ApJ 517, 40  
 Chen L.-W., Fabian A.C., Gendreau K.C., 1997, MNRAS 285, 449  
 Eke V.R., Cole S., Frenk C.S., 1996, MNRAS 282, 263  
 Gilli R., Salvati M., Hasinger G., 2001, A&A 366, 407  
 Hasinger G. et al. 2001, A&A 365, L45  
 Helsdon S.F., Ponman T.J., 2000, MNRAS 315, 356  
 Jansen F. et al. 2001, A&A 365, L1  
 Katayama H., Takahashi I., Ikebe Y., Matsushita K., Tanaka Y., Freyberg M., 2002, these proceedings (astro-ph/0201440)  
 Miyaji T., Ishisaki Y., Ogasaka Y., Ueda Y., Freyberg M.J., Hasinger G., Tanaka Y., 1998, A & A 334, L13  
 Mohr J.J., Evrard A.E., Fabricant D.G., Geller, M.J., 1995, ApJ 447, 8  
 Page M.J., 1998, MNRAS 298, 537

- Parmar A.N., Guainazzi M., Oosterbroek T., Orr A., Favata F., Lumb D., Malizia A., 1999, A & A 345, 611  
 Pierre M. et al. 2001, ESO Messenger 105, 32  
 Refregier A., Valtchanov I., Pierre M., 2001, A&A submitted (astro-ph/0109529)  
 Tozzi P., and the CDFS Team, 2002, in Proceedings of "Where's the Matter", eds. L. Tresse & M. Treyer, in press (astro-ph/0111036)  
 Valtchanov I., Pierre M., Gastaud R., 2001, A&A 370, 689  
 Xue Y.-J., Wu X.-P., 2000, ApJ 538, 65